

# Ka-Band Monopulse Antenna Pointing Calibration Using Wideband Radio Sources

Chau Buu,\* Jesus Calvo,† Tsan-Huei Cheng,\* and Manuel Vazquez†

A new method of performing a system end-to-end monopulse antenna calibration using widely available wideband astronomical radio sources is presented as an alternative to the current method of using a spacecraft signal. Current monopulse calibration requires a spacecraft carrier signal to measure amplitude and phase differences in the monopulse feed and low-noise amplifiers (LNAs). The alternative method presented here will allow the ground station to perform monopulse calibrations during maintenance periods instead of spacecraft track time, and provide an end-to-end system check-out capability without requiring a spacecraft signal. In this article, we give an overview of the current calibration approach, describe a new method for calibrating with radio sources, and present results from field testing of this new method.

## I. Introduction

The Ka-band monopulse pointing system is used in the Deep Space Network (DSN) to obtain accurate pointing at Ka-band while maximizing amplitude stability, and has been presented extensively in [1]. The monopulse pointing system is composed of the antenna, monopulse feed, low-noise amplifiers (LNAs), downlink tracking and telemetry (DTT), and antenna pointing control (APC), as shown in Figure 1. The monopulse feed produces the main signal, which is used to recover tracking and telemetry data from the spacecraft signal, and the error signal, which is used along with the main channel to calculate antenna pointing corrections. To correctly calculate the pointing errors from the error signal, a monopulse system end-to-end calibration is first required to remove the amplitude and phase differences between the main and error channels that are introduced by independent signal processing and transmission in the monopulse feed and downlink electronics (LNAs, RF-IF downconverters, fiber-optic equipment, and receiver):

- (1) The amplitude and phase differences between the signal paths from LNA input to receiver input are measured by injecting a common test signal at the inputs of both main and error channel LNAs. This calibration is performed as part of the pretrack activities prior to each monopulse track. The DTT receiver stores these values for use during monopulse tracking.

---

\* Communications Ground Systems Section.

† Madrid Deep Space Communications Complex, Madrid, Spain.

The research described in this publication was carried out by the Jet Propulsion Laboratory, California Institute of Technology, under a contract with the National Aeronautics and Space Administration. © 2010 California Institute of Technology. Government sponsorship acknowledged.

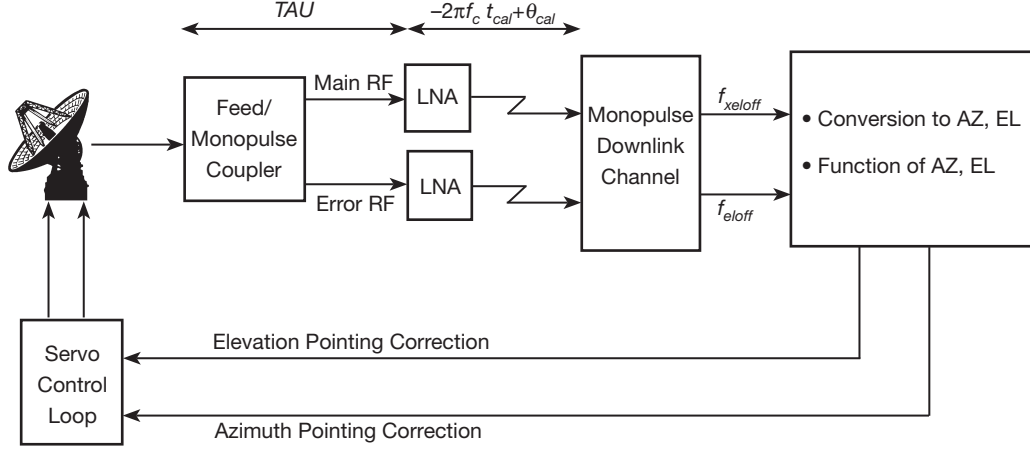


**Figure 1. Monopulse pointing system.**

- (2) Since the calibration in Equation (1) does not include the path between the monopulse coupler and LNA, a second calibration is required to measure the phase difference in this portion of the signal path. A signal source in the far-field of the antenna is required for this calibration (referred to as an on-point calibration or  $TAU$  measurement). Currently, a spacecraft signal is used as the signal source. This phase calibration ( $TAU$ ) includes the phase difference between signal paths from monopulse coupler input to LNA, the distortion due to aberration effects ( $\phi_{aberr}$ ), and the angular position of the monopulse feed within the antenna pedestal ( $\tau$ ). In theory, the  $TAU$  measurement should only need to be performed once for each station and spacecraft, but Ka-band monopulse tracks with Cassini and Mars Reconnaissance Orbiter have shown that the  $TAU$  value can change significantly over time, causing the antenna to go off-point when monopulse closed-loop tracking is enabled. One known cause for the drift in  $TAU$  was the presence of very small leaks of air at the mica windows in the LNA package. These leaks create a thin layer of ice at the waveguides that changes the propagation factor of the vacuum and hence the phase of the signal paths. This change in  $TAU$  over time in turn requires that an on-point calibration be performed occasionally before a monopulse tracking pass.

Since the on-point calibration requires introduction of significant pointing offsets, which degrade the performance of the downlink signals at X-band and Ka-band, spacecraft missions have been reluctant to provide time for the procedure. In addition, the on-point calibration can be error-prone due to the complexity of the process. It is then desired to find a method for calibrating the system in advance using widely available broadband radio sources. Using radio sources also provides the ability to perform an end-to-end checkout of the monopulse system without requiring a spacecraft downlink signal.

The first section of this article reviews the current on-point calibration procedure with a spacecraft signal. The remaining sections describe the approach for an on-point calibration with a radio source, and present the results from field testing of this approach.

## II. On-Point Calibration with a Spacecraft Carrier Signal

Following downconversion to the appropriate intermediate frequency (IF) and analog-to-digital conversion, the main and error signals at the input of the receiver are

$$x_m(t) = \sqrt{2P} \cos(2\pi f_c t + \theta_c) \quad (1)$$

$$x_e(t) = \sqrt{2P} A_{cal} \gamma \theta_F \cos(2\pi f_c (t - t_{cal}) + \theta_c + \theta_{cal} + \phi_F) \quad (2)$$

where

$P$  = received signal power

$(f_c, \theta_c)$  = carrier frequency and phase of received signal

$(A_{cal}, \theta_{cal}, t_{cal})$  = amplitude, phase, and time delay variations due to signal routing

$(\theta_F, \phi_F)$  = azimuth and elevation angle of signal arrival at the feed (in spherical coordinate system referenced to the feed), used for pointing corrections

$\gamma$  = sensitivity factor of the monopulse feed

Prior to the on-point calibration, the amplitude difference ( $A_{cal}$ ) and total phase difference ( $-2\pi f_c t_{cal} + \theta_{cal}$ ) are estimated by injecting a common carrier test signal at the input of the main and error channel LNAs. The frequency of the carrier test signal should be close to the spacecraft downlink frequency.

The receiver main signal  $x_m(t)$  is demodulated in-phase (I) and quadrature (Q) by the numerically controlled oscillator (NCO) outputs  $\cos(2\pi f_c t + \theta_c)$  and  $\sin(2\pi f_c t + \theta_c)$ , and tracked by a phase-locked loop. The error signal  $x_e(t)$  is demodulated in-phase (I) and quadrature (Q) by the NCO outputs  $\cos(2\pi f_c t + \theta_c - 2\pi f_c t_{cal} + \theta_{cal})$  and  $\sin(2\pi f_c t + \theta_c - 2\pi f_c t_{cal} + \theta_{cal})$  using the frequency and phase estimated by the main channel phase-locked loop.

Following the demodulation and half-band filter (HBF) to remove the double-frequency terms, the demodulated Q and I error signals are accumulated over  $N$  samples by the integrate-and-dump filter, and normalized by the estimate of  $\frac{N}{2} \sqrt{2P} A_{cal} \gamma$ . The resulting signals

$$f_{x\text{eloff}} = -\theta_F \sin(\phi_F) \quad (3)$$

$$f_{\text{eloff}} = \theta_F \cos(\phi_F) \quad (4)$$

are accumulated over 40 ms (25-Hz rate) and sent to the APC. In the APC,  $f_{x\text{eloff}}$  and  $f_{\text{eloff}}$  are derotated and scaled to obtain the elevation and cross-elevation angles in the antenna coordinates as follows:

$$\begin{pmatrix} x_{\text{eloff}} \\ \text{el}_{\text{off}} \end{pmatrix} = BDF \begin{pmatrix} \cos(\phi\Delta) & -\sin(\phi\Delta) \\ \sin(\phi\Delta) & \cos(\phi\Delta) \end{pmatrix} \begin{pmatrix} f_{x\text{eloff}} \\ f_{\text{eloff}} \end{pmatrix} \quad (5)$$

where

$xel_{off}$  = estimate of the pointing error in the cross-elevation axis  
 $el_{off}$  = estimate of the pointing error in the elevation axis  
 $BDF$  = antenna amplification factor  
 $\phi_{\Delta} = AZ - EL + TAU$   
 $TAU = -\tau + \phi_{aberr}$   
 $AZ$  = current antenna azimuth angle  
 $EL$  = current antenna elevation angle  
 $\tau$  = parameter dependent upon the physical location of the feed  
 $\phi_{aberr}$  = phase distortion due to aberration effects

To perform the on-point calibration, conscan is enabled to boresight the antenna to the spacecraft signal. From boresight, a known offset in elevation or cross-elevation is introduced. Since  $AZ$ ,  $EL$ ,  $f_{xel_{off}}$ , and  $f_{el_{off}}$  are known,  $TAU$  can be found by solving Equation (5) such that  $-el_{off}$  and  $-xel_{off}$  are equal to the introduced offsets. For example, if the antenna is offset by +0.007 deg in elevation and 0 deg in cross-elevation, then the desired  $el_{off}$  and  $xel_{off}$  are -0.007 deg and 0 deg, respectively. In practice, a series of measurements at different offsets is used to ensure validity of the  $TAU$  measurement.

### III. On-Point Calibration with a Radio Source

An alternative approach is to use a wideband radio source to provide correlated noise in the main and error channels of the receiver, allowing the phase and time delay difference to be measured.

Prior to the on-point calibration, the amplitude difference ( $A_{cal}$ ) and total phase difference ( $-2\pi f_c t_{cal} + \theta_{cal}$ ) are estimated by injecting a common carrier test signal at the input of the main and error channel LNAs. The frequency of the carrier test signal should be close to the spacecraft downlink frequency for which the  $TAU$  is being measured.

The radio source is modeled as  $\sqrt{2kT_q B} A(t)$ , where  $k$  is Boltzmann's constant,  $T_q$  is the contribution to the antenna noise temperature by the radio source,  $B$  is the receiver noise bandwidth, and  $A(t)$  is a random process with mean-square value  $E\{A^2\} = 1$ . The inputs to the receiver are the main ( $x_m(t)$ ) and error ( $x_e(t)$ ) signals

$$x_m(t) = \sqrt{2kT_q B} A(t) \cos(2\pi f_c t + \theta_c) \quad (6)$$

$$x_e(t) = \sqrt{2kT_q B} A(t - t_{cal}) A_{cal} \gamma \theta_F \cos(2\pi f_c (t - t_{cal}) + \theta_c + \theta_{cal} + \phi_F) \quad (7)$$

where

$(f_c, \theta_c)$  = carrier frequency and phase of received signal  
 $(A_{cal}, \theta_{cal}, t_{cal})$  = amplitude, phase, and time delay variations due to signal routing  
 $(\theta_F, \phi_F)$  = azimuth and elevation angle of signal arrival at the feed (in spherical coordinate system referenced to the feed)  
 $\gamma$  = sensitivity factor of the monopulse feed

Cross-correlation techniques for estimating phase and time delay differences are evaluated for implementation in the DTT, based on time-domain and frequency-domain approaches that have been presented in the literature [2].

#### A. Time-Domain Approach

The time-domain approach for estimating phase and time delay is shown in Figure 2. The receiver main signal  $x_m(t)$  is multiplied by the NCO outputs  $\cos(2\pi\hat{f}_c t + \theta_c)$  and  $\sin(2\pi\hat{f}_c t + \theta_c)$ , where  $\hat{f}_c$  is the estimate of  $f_c$ . The main I and Q demodulation signals are

$$V_m(t) = \frac{1}{2}\sqrt{2kT_q B} A(t) \cos(2\pi\Delta f_c t) \quad (8)$$

$$U_m(t) = -\frac{1}{2}\sqrt{2kT_q B} A(t) \sin(2\pi\Delta f_c t) \quad (9)$$

where  $\Delta f_c = f_c - \hat{f}_c$ . Similarly, the receiver error signal  $x_e(t)$  is demodulated by the error NCO outputs  $\cos(2\pi\hat{f}_c t + \theta_c - 2\pi\hat{f}_c t_{cal} + \theta_{cal})$  and  $\sin(2\pi\hat{f}_c t + \theta_c - 2\pi\hat{f}_c t_{cal} + \theta_{cal})$ . The error I and Q demodulation signals are

$$V_e(t) = \frac{1}{2}\sqrt{2kT_q B} A(t - t_{cal}) A_{cal} \gamma \theta_F \cos(2\pi\Delta f_c(t - t_{cal}) + \phi_F) \quad (10)$$

$$U_e(t) = -\frac{1}{2}\sqrt{2kT_q B} A(t - t_{cal}) A_{cal} \gamma \theta_F \sin(2\pi\Delta f_c(t - t_{cal}) + \phi_F) \quad (11)$$

The phase and time delay differences between the main and error channels can be obtained by computing the cross-correlation function

$$c_{em}(\nu) = \langle y_e(t) y_m^*(t - \nu) \rangle \quad (12)$$

where

$$y_m(t) = V_m(t) + jU_m(t)$$

$$y_e(t) = V_e(t) + jU_e(t)$$

The cross-correlation  $|c_{em}(\nu)|$  is accumulated over  $N$  samples (1 s). The magnitude of  $|Nc_{em}(\nu)|$  has a peak at  $\nu = t_{cal}$ , where

$$c_{em}(t_{cal}) \simeq \frac{1}{2}kT_q B A_{rr} A_{cal} \gamma \theta_F e^{-j\phi_F} \quad (13)$$

and  $A_{rr}$  is the autocorrelation of radio source signal at  $\nu = t_{cal}$ . The imaginary and real components of  $|Nc_{em}(t_{cal})|$  are normalized and sent to the APC

$$f_{x\text{eloff}} = -\theta_F \sin(\phi_F) \quad (14)$$

$$f_{\text{eloff}} = \theta_F \cos(\phi_F) \quad (15)$$

In the APC,  $f_{x\text{eloff}}$  and  $f_{\text{eloff}}$  are derotated and scaled to obtain the elevation and cross-elevation angles using Equation (5). The antenna calibration and measurement equipment (ACME) is used to boresight to the radio source. From boresight, a known offset in elevation or cross-elevation is introduced.  $TAU$  can then be found using the same procedure as with a spacecraft signal.

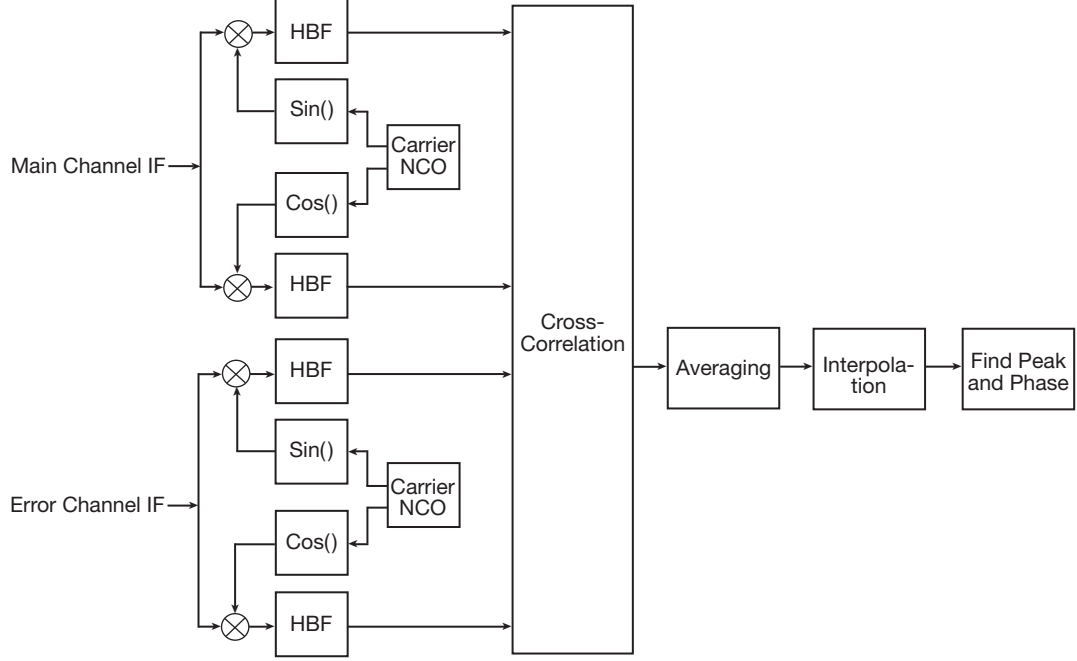


Figure 2. Time-domain approach.

### B. Frequency-Domain Approach

The frequency-domain approach was also evaluated for implementation since it is a computationally efficient approach for computing the cross-correlation. The frequency-domain approach for estimating phase and time delay is shown in Figure 3. For simplicity, we assume that the signals have been normalized by the total signal power. The Fourier transforms of the main and error signals are

$$Y'_m(f) = \frac{1}{2} \sqrt{2kT_q B} [R(f - \Delta f_c) + R^*(-f - \Delta f_c)] \quad (16)$$

$$Y'_e(f) = \frac{1}{2} \sqrt{2kT_q B} \phi_F [R(f - \Delta f_c) e^{-j(2\pi(f - \Delta f_c)t_{cal} + \phi_F)} + R^*(-f - \Delta f_c) e^{-j(2\pi(-f - \Delta f_c)t_{cal} + \phi_F)}] \quad (17)$$

where

$R(f)$  = Fourier transform of radio source signal

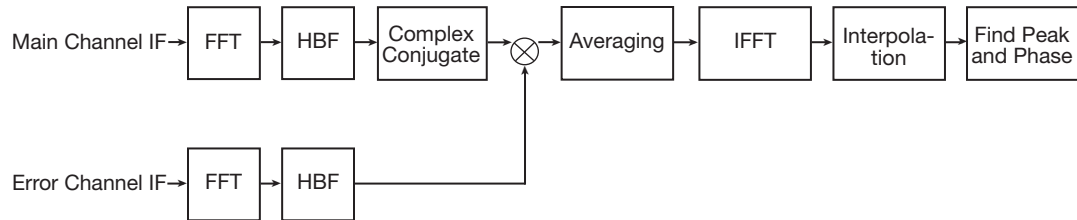


Figure 3. Frequency-domain approach.

The signals  $Y'_m$  and  $Y'_e$  are filtered by the HBF, and the outputs are

$$Y_m(f) = \frac{1}{2} \sqrt{2kT_q B} R(f - \Delta f_c) \quad (18)$$

$$Y_e(f) = \frac{1}{2} \sqrt{2kT_q B} \phi_F R(f - \Delta f_c) e^{-j(2\pi(f - \Delta f_c)t_{cal} + \phi_F)} \quad (19)$$

The Fourier transform of the cross-correlation function is

$$C_{em}(f) = Y_e(f) Y_m^*(f) \quad (20)$$

$$= \frac{1}{2} kT_q B \phi_F |R(f - \Delta f_c)|^2 e^{-j(2\pi(f - \Delta f_c)t_{cal} + \phi_F)} \quad (21)$$

The inverse transform of  $C_{em}(f)$  is computed to obtain the cross-correlation  $c_{em}(t)$ . From here, the procedure for evaluating  $f_{xeloff}$ ,  $f_{eloff}$ , and  $TAU$  is the same as in Section III.A.

### C. Simulation Results

Simulations are performed using the CoWare Signal Processor Workbench (SPW). Modeled radio sources are 2.5 K and 1 K, based on available Ka-band sources such as 2C273 (2.5 K), 3C274 (2.2 K), and 3C84 (2 K). Following downconversion, the main and error input signals are sampled at a rate  $f_s = \frac{1}{T_s} = 2B = 160$  MHz. The main and error channels have additive noise with spectral density of  $N_{o,m} = kT_{sys,m}$  and  $N_{o,e} = kT_{sys,e}$ , respectively, where  $T_{sys,m}$  is the main channel system noise temperature ( $\sim 40$  K), and  $T_{sys,e}$  is the error channel system noise temperature ( $\sim 55$  K). The noise terms are Gaussian with zero mean and variance  $\frac{N_{o,m}}{2T_s}$  and  $\frac{N_{o,e}}{2T_s}$ , respectively.

In order to generate a time delay that is not a multiple of the sampling rate, the signal is first upsampled, then downsampled at a simulation clock speed of 640 MHz. Therefore, the time delay in the simulation is in integer multiples of the simulation clock period (1.5625 ns).

The integration time is 0.1 s and 0.2 s for the 2.5-K and 1-K radio source, respectively. The simulation results for the time-domain and frequency-domain approaches are shown in Tables 1 and 2.

The simulation results show that the measured phase delays agree well with the expected values. The error should be less than 45 deg for monopulse to acquire successfully, although the desired measurement accuracy is  $\pm 25$  deg for a shorter acquisition time.

Since the effective sample rate following the HBF is 80 MHz, the resolution of the time delay estimate is 12.5 ns, but a resolution of 0.78 ns is achieved through an interpolation process. To compensate for time delay, we simulated an 8-point sinc function digital filter. The performance of the filter is verified by injecting an input sinewave test signal into both main and error channels. A time delay of 4.8 ns is introduced in the path of the error channel. The measured time delay error is shown in Table 3.

**Table 1. Comparison of expected and measured time and phase delay for 2.5 K.**

Approach, Section	Expected Time Delay, ns	Measured Time Delay, ns	Expected Phase Delay, deg	Measured Phase Delay, deg
III.A	34.375	34.00	195	194.60
III.B	34.375	33.98	195	194.66
III.A	4.68	5.07	23.5	22.2
III.B	4.68	5.07	23.5	23.13
III.A	12.5	12.1	88.0	88.01
III.B	12.5	12.1	88.0	88.21
III.A	20.31	20.61	107.5	109.67
III.B	20.31	20.60	107.5	108.53

**Table 2. Comparison of expected and measured time and phase delay for 1 K.**

Approach, Section	Expected Time Delay, ns	Measured Time Delay, ns	Expected Phase Delay, deg	Measured Phase Delay, deg
III.A	34.375	34.00	195	194.60
III.B	34.375	*	195	*

\*Not processed due to space limitation in SPW.

**Table 3. Filter performance.**

Center Frequency, MHz	Time Delay Error, ns	Total Phase Error, deg
10	0.052	0.19
20	0.079	0.57
40	0.114	1.64
60	0.151	3.27
70	0.288	7.24

#### IV. Implementation and Field Test Results

The calibration method was first implemented using the Radio Science Receiver (RSR) as an open-loop monopulse receiver. The data were downconverted and filtered by the RSR, then correlated in software using an external application. The selected channel bandwidth was 1 MHz, which ensured that the peak was at the center and removed the need for a full correlation. The phase of the correlation data was derotated in a dedicated software program, and the *TAU* was estimated by an on-point calibration using a radio source. Next, the cross-correlation function was implemented in field-programmable gate array (FPGA) on the DTT digital signal processor (DSP) board. Although the frequency-domain technique is more computationally efficient than the time-domain technique, the advantage of the time-domain approach is that some of the existing FPGA circuits can be re-used, thereby reducing the overall complexity of the implementation. The FPGA implementation of the cross-correlation is thus based on the approach presented in Section III.A, with time delay range of  $\pm 350$  ns and resolution of 1.5625 ns.



We initially investigated time delay compensation to minimize the loss in the magnitude of the cross-correlation, but field test results showed that this was not required for the set of sources that were used for the calibration. Therefore, the time delay correction was not implemented for the current system.

A test was performed at DSS-55 on DOY 201, 2010, to verify that the  $f_{x\text{eloff}}$  and  $f_{\text{eloff}}$  values changed as expected when applying known antenna position offsets from beam peak. Figure 4 shows the cross-correlation measurements using radio source DR21 (2.3 K). The recorded  $f_{x\text{eloff}}$  and  $f_{\text{eloff}}$  data (prior to normalization) show good clustering at four points 90 deg apart for antenna cross-elevation and elevation position offsets of (7 mdeg, 0 deg), (0 deg, +7 mdeg), (-7 mdeg, 0 deg), and (0 deg, -7 mdeg) from boresight. The measurements are almost zero-centered, which is desired.

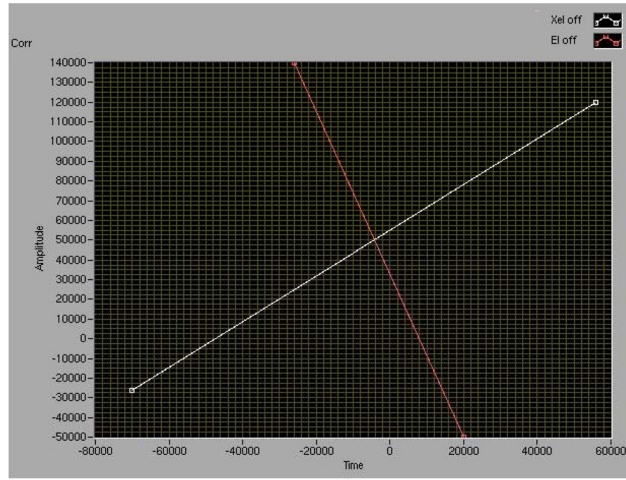
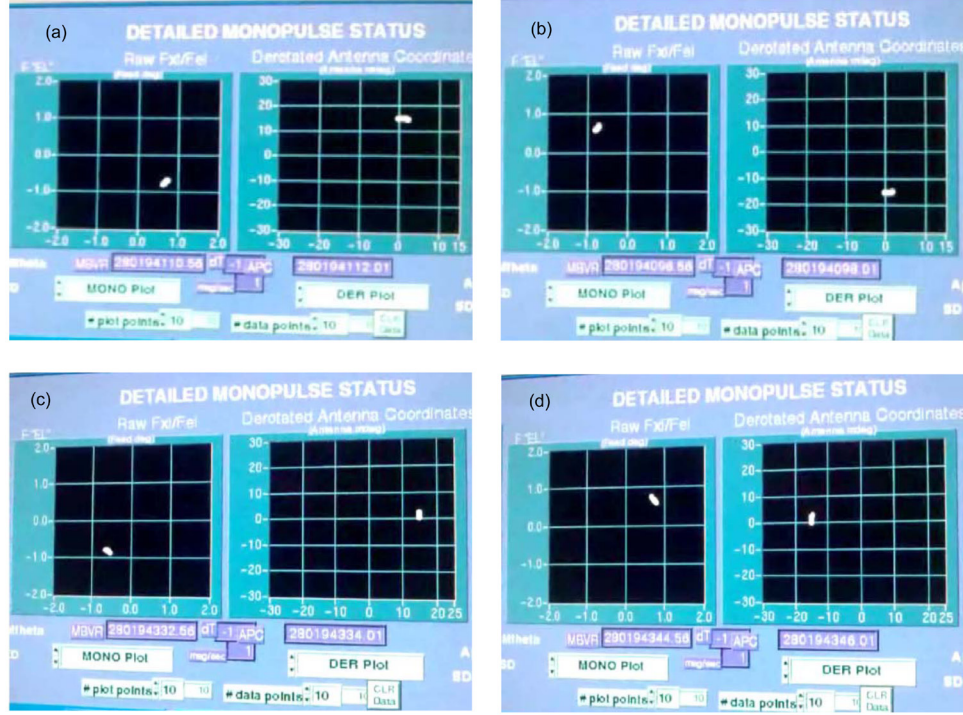


Figure 4.  $f_{x\text{eloff}}$  and  $f_{\text{eloff}}$  (unnormalized) measurements at DSS-55.

On DOY 207, 2010, a test was conducted at DSS-55 to measure  $TAU$  using the radio source 3C454.3 (5.1 K). At the start of the test, the amplitude and phase differences between the LNA and receiver are estimated by injecting a common carrier test signal. The frequency of the carrier test signal was selected to be close to the Cassini downlink frequency (32.03 GHz). Prior to the on-point calibration, the  $f_{x\text{eloff}}$  and  $f_{\text{eloff}}$  data are first corrected for atmospheric effects by pointing the antenna off-source (see Section V for more details). The  $TAU$  measured using the radio source was 60 deg, compared to a  $TAU$  of 70 deg used for current Cassini monopulse tracks. The  $TAU$  of 70 deg is an average of the  $TAUs$  measured from the 1-way downlink frequency and 2/3-way downlink frequency. A source of the error is that the data that were sent to the APC were not from the peak cross-correlation data (the data from the peak were logged in the receiver, and these data were 10 deg off from the data that were sent to the APC). If this error is removed, the difference between the  $TAU$  measured from the radio source and the average  $TAU$  measured from the spacecraft signal is very small. The measured time delay was -17 ns.

Figures 5(a) through 5(d) show snapshots of the Antenna Maintenance Terminal (AMT) monopulse display for four antenna position offsets. The left plot on the monopulse display



**Figure 5. DSS-55 derotated measurements for (a)  $-7$  mdeg offset in elevation; (b)  $+7$  mdeg offset in elevation; (c)  $-7$  mdeg offset in cross-elevation; and (d)  $+7$  mdeg offset in cross-elevation.**

shows  $f_{eloff}$  and  $f_{xeloff}$  measurements, while the right plot shows derotated data in antenna coordinates. With a  $TAU$  of 60 deg, all four antenna position offsets resulted in the correct derotated data:

- (1) In Figure 5(a), applying a  $-7$  mdeg position offset in elevation resulted in derotated offset of EL of 0 mdeg, and XEL of  $+15$  mdeg (the amplitude is off by a factor of 2, but no work was done on the gain computation).
- (2) In Figure 5(b), applying a  $+7$  mdeg position offset in elevation resulted in derotated offset of EL of 0 mdeg, and XEL of  $-15$  mdeg.
- (3) In Figure 5(c), applying a  $-7$  mdeg position offset in cross-elevation resulted in derotated offset of EL of  $+15$  mdeg, and XEL of 0 mdeg.
- (4) In Figure 5(d), applying a  $+7$  mdeg position offset in cross-elevation resulted in derotated offset of EL of  $-15$  mdeg, and XEL of 0 mdeg.

The  $TAU$  measurement was also performed at DSS-26 using radio source 3C274 (1.8 K) on DOY 201, 2010. The  $TAU$  measured using the radio source was  $-160$ , compared to a  $TAU$  of  $-130$  deg used for current Cassini monopulse tracks. The  $TAU$  of  $-130$  deg is an average of the  $TAUs$  measured from the 1-way downlink frequency and 2/3-way downlink frequency. The data used for the  $TAU$  computation were  $\sim 10$  deg from the peak cross-correlation data. If this error is removed, the difference between the  $TAU$  measured from the radio source and the average  $TAU$  measured from the spacecraft signal is approximately 20 deg.

Figure 6(a) shows the  $f_{x\text{eloff}}$  and  $f_{\text{eloff}}$  data prior to atmospheric correction, Figure 6(b) shows the  $f_{x\text{eloff}}$  and  $f_{\text{eloff}}$  data following atmospheric correction, and Figure 6(c) shows the derotated data for antenna cross-elevation and elevation position offsets of (7 mdeg, 0 deg), (0 deg, +7 mdeg), (-7 mdeg, 0 deg), and (0 deg, -7 mdeg) from boresight. The derotated measurement was done during post-processing (i.e., the data shown in the plot are not from the APC display).

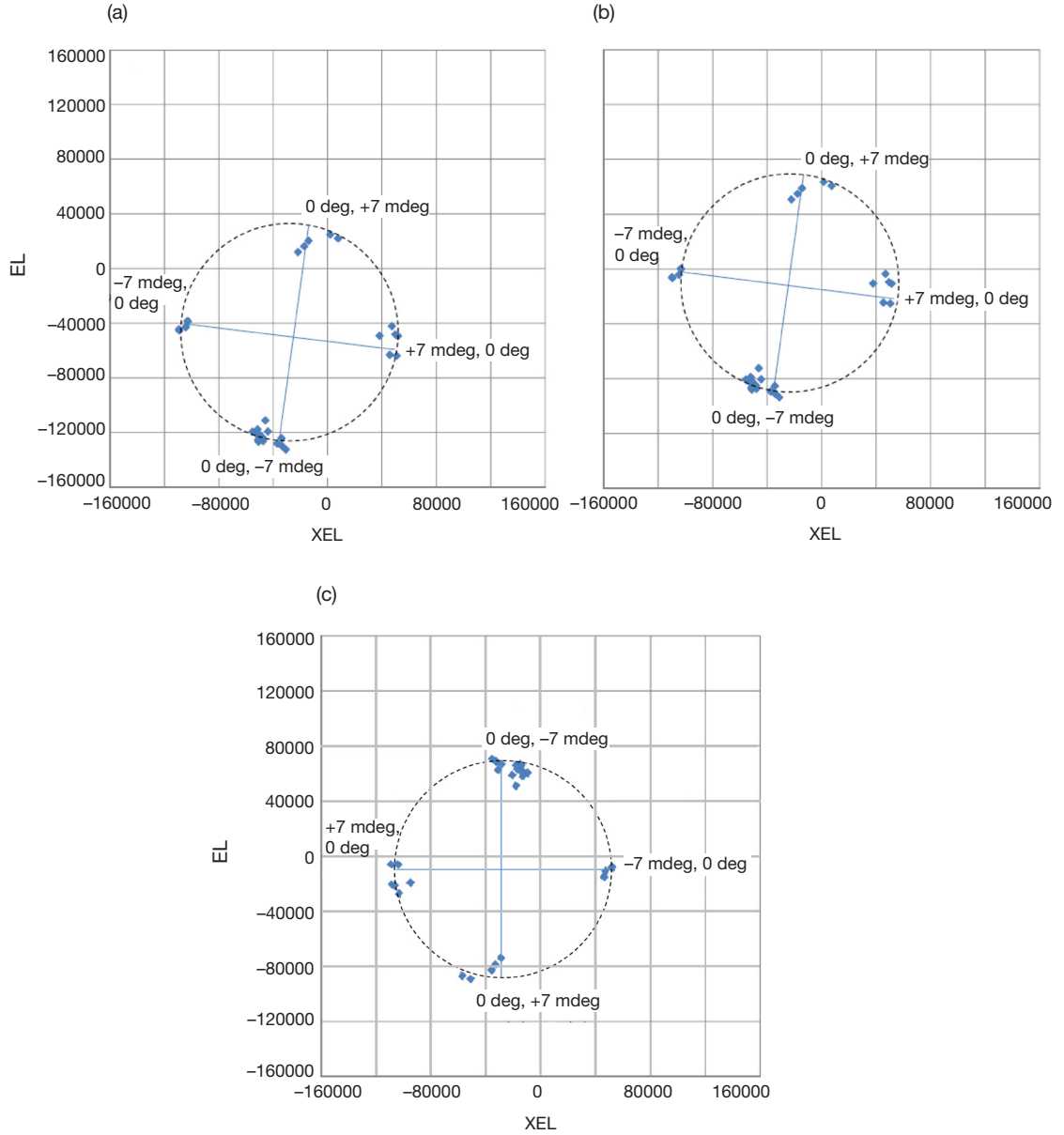


**Figure 6. DSS-26 measurements for (a)  $f_{x\text{eloff}}$  and  $f_{\text{eloff}}$  (unnormalized) prior to atmospheric correction; (b)  $f_{x\text{eloff}}$  and  $f_{\text{eloff}}$  (unnormalized) following atmospheric correction; and (c) post-processed derotated data.**

## V. Atmospheric Correction

Testing showed that errors in the  $TAU$  measurement vary with atmospheric conditions. Testing under dry and clear sky conditions resulted in small errors in the  $TAU$  measurements. In cloudy conditions, the thermal emissions of the clouds can vary significantly over time and antenna position, making it difficult to correct for the noise contribution from the atmospheric emission. Therefore, unless the clouds contain a very low water density and their thermal emissions are negligible compared to the source temperature, the measurement can be significantly impacted, to the point of inoperability.

The system noise temperature  $T_{sys}$  can be broken down into the following main contributions:

$$T_{sys} = T_a + T_{gnd} \quad (22)$$

where

$$\begin{aligned} T_a &= \text{antenna noise temperature} = T_q + T_{bg} + T_{atm} + T_{ant} \\ T_{gnd} &= \text{ground noise temperature} = T_{LNA} + T_{rcv} \\ T_q &= \text{noise contribution from radio source} \\ T_{bg} &= \text{noise contribution from cosmic background} \\ T_{atm} &= \text{noise contribution from atmospheric emission} \\ T_{ant} &= \text{noise contribution from antenna} \\ T_{LNA} &= \text{noise contribution from LNA} \\ T_{rcv} &= \text{noise contribution from follow-on receiver electronics} \end{aligned}$$

Since only  $T_a$  is common to both main and error channels, the cross-correlation for the received system noise is

$$\begin{aligned} \text{Re}[c_{sys}(t_{cal})] + j\text{Im}[c_{sys}(t_{cal})] &= (\text{Re}[c_q(t_{cal})] + j\text{Im}[c_q(t_{cal})]) \\ &\quad + (\text{Re}[c_{bg+atm+ant}(t_{cal})] + j\text{Im}[c_{bg+atm+ant}(t_{cal})]) \end{aligned} \quad (23)$$

where

$$\begin{aligned} c_q(t) &= \text{cross-correlation from radio source} \\ c_{bg+atm+ant}(t) &= \text{cross-correlation from cosmic background, atmospheric emission, and antenna} \end{aligned}$$

To measure  $c_{bg+atm+ant}(t_{cal})$ , a cross-correlation is performed with the antenna pointed off-source (approximately 100 mdeg from boresight). The resulting real and imaginary cross-correlation values are then subtracted from  $\text{Re}[c_{sys}(t_{cal})] + j\text{Im}[c_{sys}(t_{cal})]$  to obtain  $\text{Re}[c_q(t_{cal})] + j\text{Im}[c_q(t_{cal})]$ .

## VI. Concluding Remarks

This work demonstrated that a monopulse on-point calibration can be performed using widely available Ka-band radio sources. The benefits to the DSN include eliminating the need for dedicated tracking time for the on-point calibration, reducing the probability for

the antenna to go off-point due to an error in  $TAU$ , and providing the capability to perform an end-to-end checkout of the monopulse system without a spacecraft signal.

Potential follow-up work includes making the system operational by providing formal operator directives and displays, automating the atmospheric calibration, estimating the noise powers (to accurately normalize the cross-correlation data), and compensating for the time delay. Other future work includes evaluating monopulse tracking for a broadband radio source, which can be of interest to very long baseline interferometry (VLBI) and delta-DOR users. In addition, the pointing errors derived from the monopulse system can help improve blind pointing over a wide Ka-band frequency range (similar to what is currently done for Cassini-specific Ka-band pointing predicts).

## References

- [1] M. A. Gudim, W. Gawronski, W. J. Hurd, P. R. Brown, and D. M. Strain, "Design and Performance of the Monopulse Pointing System of the DSN 34-Meter Beam-Waveguide Antennas," *Telecommunications and Mission Operations Progress Report*, vol. 42-138, Jet Propulsion Laboratory, Pasadena, California, pp. 1–29, August 15, 1999 (cover date April–June 1999). [http://ipnpr.jpl.nasa.gov/progress\\_report/42-138/138H.pdf](http://ipnpr.jpl.nasa.gov/progress_report/42-138/138H.pdf)
- [2] S. Lawrence Marple, Jr., "Estimating Group Delay and Phase Delay via Discrete-Time 'Analytic' Cross-Correlation," *IEEE Transactions on Signal Processing*, vol. 47, no. 9, pp. 2604–2607, September 1999.